Article

pubs.acs.org/Biomac

Interaction Pathways between Plasma Membrane and Block Copolymer Micelles

Zhou Guan, Liquan Wang,* and Jiaping Lin*

Shanghai Key Laboratory of Advanced Polymeric Materials, State Key Laboratory of Bioreactor Engineering, Key Laboratory for Ultrafine Materials of Ministry of Education, School of Materials Science and Engineering, East China University of Science and Technology, Shanghai 200237, China

Supporting Information

ABSTRACT: In this work, the interactions between block copolymer micelles (BCMs) and plasma membranes were investigated by performing coarse-grained molecular dynamics (CGMD) simulations. Different binding strengths between the BCMs and the membranes were tested, and four interaction pathways were discovered: attachment, semiendocytosis, endocytosis, and fusion. Endocytosis was the most efficient way for the BCMs to be taken up, and fusion could lead to cytotoxicity. Unlike rigid particles, deformation of the BCMs strongly affected the interaction pathways. We examined the effects of changing the aggregation number of the BCMs (N_{agg}), the chain length of the polymer (N_b), and the chain stiffness of the hydrophobic block (k_a), and we learned that smaller N_{agg} and lower N_b could lead to weaker cellular uptake capacities, whereas larger N_{agg} and higher N_b gave rise to higher cytotoxicities. Moreover, a weaker chain stiffness of the hydrophobic block could be more favorable for obtaining BCMs with higher internalization efficacies and lower cytotoxicities. The results of these simulations could aid in the design of BCMs with desirable cellular internalization capacities and lower cytotoxicities. Such BCMs could be useful in drug-delivery systems.

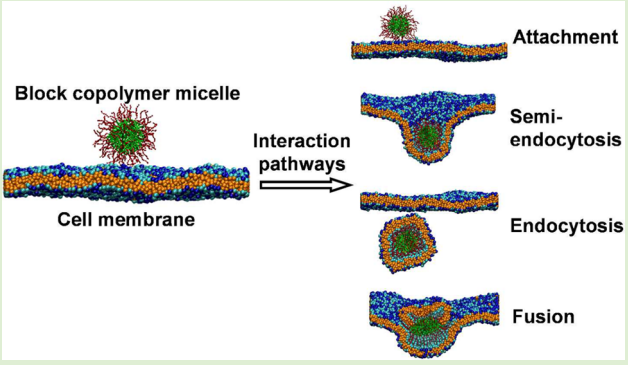

INTRODUCTION

The interactions between drug-delivery systems (DDSs) and plasma membranes are important factors that affect the in vivo lifetimes of DDSs.[1−3] When loaded with drugs, a DDS may release drugs outside of cells, or it may release inside the cells after penetrating the plasma membrane.[1,4,5] The interactions between the DDS and the plasma membrane directly influence the drug release performance and toxicity to the human body. By designing and preparing novel DDSs, the cellular uptake performances of drugs at tumor sites can be improved (e.g., higher uptake efficacy and active targeting). Many types of DDS have been developed, including polymer−drug conjugates, dendrimers, porous nanoparticles, polymer vesicles, and micelles.[6−10] The interactions between these various DDSs and the plasma membrane have different characteristics. These various interaction pathways could have influences on the cellular uptake capacity and cytotoxicity of DDS, which lead to different drug-releasing and therapeutic efficacy as consequences. Understanding these interaction behaviors is important in studies of DDSs and tumor therapies.

Although experimental investigations can suggest possible interaction pathways between DDSs and plasma membranes,[11−13] detailed information about the interactions mainly comes from theory.[14−18] For molecular-level DDSs (e.g., nanoparticles smaller than 5 nm and polymer−drug conjugates), the DDS can spontaneously translocate, sometimes through the pores of a membrane.[19−21] For example, using Monte Carlo simulations, Skolnick et al. found that hydrophobic polymers can penetrate bilayer membranes, and they showed that membrane curvature affects the translocation.[19] Another important DDS category is large rigid nanoparticles. Theoretical investigations have proven that most of these particles are internalized via endocytosis. The effects of the size, shape, and surface ligands on endocytosis have been examined explicitly.[22−27] For instance, Robert et al. simulated the passive receptor-mediated endocytosis of ligand-decorated nanoparticles by performing coarse-grained molecular dynamics (CGMD) simulations,[22] and they found that nanoparticles with isotropic shapes, higher ligand coverages, and strong binding to receptors on membranes have greater endocytosis capacities. The simulation method proposed by Cooke and coworkers maintains the principal properties of the cell membrane (e.g., bending modulus, surface tension, and diffusion constant).[28] This model has been successfully used to study the endocytosis of both rigid and soft nanoparticles.[22,50,51] Unlike the rigid particles, soft DDS particles can be deformed during the interaction, which can produce different particle−membrane interactions.[29−32] For example,

Received: November 12, 2016
Revised: January 24, 2017
Published: January 26, 2017

DOI: 10.1021/acs.biomac.6b01674
Biomacromolecules 2017, 18, 797−807

Sun et al. prepared soft particles (polymeric cores and lipid shells) with different rigidities and studied their cellular uptakes.[29] The more rigid particles were endocytosed more easily. They confirmed the result by performing molecular dynamics (MD) simulations.[29] The details about the interactions between the soft DDS particles and plasma membranes have also been explored.[18,33−35] For instance, Yue and co-workers investigated the interactions between vesicles and membranes by performing dissipative particle dynamics (DPD) simulations.[33] Five possible interaction pathways were found. The results are helpful for understanding the drug-delivery process for vesicles loaded with hydrophilic drugs. In addition to vesicles, block copolymer micelles (BCM) are an important class of soft DDS particles.[5,7,36−38] Unlike vesicles, BCMs have hydrophobic cores and hydrophilic shells, which allow them to carry hydrophobic drugs. This unique structure may affect the cellular internalization performance. Many experiments have been conducted to investigate the drug-delivery performance of BCMs. Block copolymers with various physical and chemistry properties were used to prepare BCMs with desirable cellular uptake performance and low cytotoxicity.[39−45] Several parameters of polymers and micelles (e.g., degree of polymerization and hydrophobic/hydrophilic volume fraction) strongly affect the cellular internalization results.[46−49] However, due to the limitations of current experimental techniques, little is known about BCM−membrane interaction pathways. For example, it is not known how the BCM penetrates the membrane and enters the cell. Knowledge of these interaction behaviors could aid the design of novel BCMs with improved cellular uptake capacity, and it could enable new DDS applications. Simulations such as CGMD can provide deep insight into the interactions between DDS particles and plasma membranes, and information from simulations can help address challenges in drug delivery.[22,28,50,51]

In this study, we performed CGMD simulations to investigate the interactions between micelles self-assembled from amphiphilic diblock copolymers and plasma membranes. We predicted various BCM−membrane interaction pathways, and we learned that the deformation of BCMs and the energy expended during the interaction have significant effects. We investigated the effects of the three most important BCM structural parameters on the interaction pathways: the aggregation number of the BCM (N_{agg}), the chain length of the polymers (N_b), and the rigidity of the hydrophobic block of the polymers (k_a). The simulation results showed good agreement with existing experimental observations.

MODEL AND METHODS

We constructed a system containing a plasma membrane and a micelle that was self-assembled from A_mB_n diblock copolymers. The models are illustrated in Figure 1a−c. Figure 1a shows the details of the A_mB_n diblock copolymer model, in which the hydrophobic and the hydrophilic segments are denoted by m green beads and n red beads, respectively. By varying the values of m and n, we obtained copolymers with varying degrees of polymerization. The BCMs used in the simulations were all picked up from additional simulations (see Supporting Information, Section 1). The BCMs have equilibrium structures in aqueous systems in our simulations. The bilayer plasma membrane was composed of phospholipids, as illustrated in Figure 1b. According to the solvent-free model proposed by Cooke et al.,[28] the phospholipids are coarse-grained to three beads connected by bonds. The head bead of each lipid is

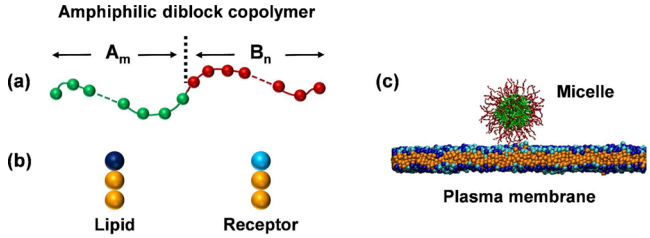

Figure 1. Models used in the simulations. (a) Amphiphilic diblock copolymer (A_mB_n), in which A and B block are hydrophobic and hydrophilic, denoted by green and red beads, respectively. m and n denote to the number of beads in the A and B blocks; (b) phospholipid and receptor; (c) initial status of the system, in which the self-assembled BCM is set above the plasma membrane.

hydrophilic, denoted in purple. The two tail beads are hydrophobic, denoted in orange. Specific amounts of lipids in the membrane are receptors, whose head beads are shown in blue. These lipids can bind to the hydrophilic shell of the BCM. The BCM was set to make contact with the membrane, as shown in Figure 1c.

For the lipids and polymer chains, the bonds linking two neighboring beads are defined by a finite extensible nonlinear elastic (FENE) potential,

$$E_{bond}(r) = -1/2k_b r_b^2 \ln[1 - (r/r_b)^2] \quad (1)$$

where the strength $k_b = 30\varepsilon_0/\sigma^2$ and the maximum extent of the bond $r_b = 1.5\sigma$. ε_0 and σ are the energy and the length units, respectively. Additionally, a harmonic spring potential is applied to two next-nearest neighboring beads (i.e., two beads bonded to the same bead) to maintain their straight shape:

$$E_{bend}(r) = 1/2k_a(r - r_a)^2 \quad (2)$$

The strength $k_a = 10\varepsilon_0/\sigma^2$ and the equilibrium bond distance $r_a = 4\sigma$. For polymers, this potential was also applied to the beads of the A block if the hydrophobic blocks were rigid. r_a was set to 4σ. Because the maximum length of two next-nearest neighboring beads is 3σ (the double of maximum bond length 1.5σ), this harmonic spring potential with $r_a = 4\sigma > 3\sigma$ exhibits a tendency to push the two beads and straighten the lipids.[28] Whereas for polymers, this potential was also applied to two next-nearest neighboring beads of the A block if the hydrophobic blocks were rigid, where $r_a = 4\sigma$ and the value of k_a was varied. Higher k_a values are associated with stronger rigidity.

In this model, the potentials between all beads are represented as follows:[28]

$$E_{inter}(r) = \begin{cases} 4\varepsilon_0[(\lambda_{ij}\sigma/r)^{12} - (\lambda_{ij}\sigma/r)^6], & r < r_{cut} \\ -\varepsilon_{ext}\cos^2[\pi(r - r_{cut})/2/(r_{ext} - r_{cut})], & r_{cut} \le r \le r_{ext} \\ 0, & r > r_{ext} \end{cases} \quad (3)$$

The first part of the function is a Lennard-Jones potential. ε_0 is the interaction strength, which was set as the energy unit in the present work. σ is the length unit, and the cutoff distance $r_{cut} = 2^{1/6}\lambda_{ij}\sigma$. The values of λ_{HH} and λ_{HT} were both set as 0.95, where the subscript H and T denote the head/receptor and the tail beads of the phospholipids, respectively. For other beads, the values of λ were all set to 1. The middle piece of the function represents the attractions between all of the tail beads of the lipids, the hydrophobic (A) blocks, and the binding between

DOI: 10.1021/acs.biomac.6b01674
Biomacromolecules 2017, 18, 797−807

hydrophilic (B) blocks and receptors. In contrast with the attraction part of LJ potential, the potential width of the middle piece can be easily tuned by setting the value of $r_{ext} - r_{cut}$. Previous work has demonstrated that tuning the potential width is the key to obtaining a fluid bilayer state and the potential with a broad attractive width can stabilize the fluid bilayer phase.[28] This potential can capture the effects of solvent exclusion and lipid−lipid interactions in bilayers. Although other potentials with a broad attractive width may share the important property of exhibiting a stable fluid bilayer phase, the present middle piece is one of several successful potentials. For tail beads, the binding strength $\varepsilon_{ext} = \varepsilon_0$, and the cutoff distance $r_{ext} = 3.65\sigma$, which are supposed to be the optimal values for maintaining a plasma membrane. For the interaction between hydrophobic blocks, $r_{ext} = 3.02\sigma$. For the pair of B blocks and the receptor, r_{ext} was also set to 3.02σ, which is a value that has been used in simulations by Vácha et al.[22] ε_{ext} was varied in the simulations.

The simulations were performed under constant temperature. A Langevin thermostat, developed by Schneider et al. was used.[52] The beads were coupled to a heat bath, and the equations of motion are expressed as follows:[53]

$$m_i\mathbf{a}_i = \mathbf{F}_i - \Gamma\mathbf{v}_i + \mathbf{W}_i(t) \tag{4}$$

where m_i, $\mathbf{a}_i$, and $\mathbf{v}_i$ are the mass, acceleration, and velocity of the ith bead. $\mathbf{F}_i$ is the force acting on the ith bead, which is calculated based on the potential energies consisting of $E_{bond}(r)$, $E_{bend}(r)$, and $E_{inter}(r)$. Γ is the friction constant. In the Langevin dynamics, the effect of the solvent molecules is implicitly treated by the noise term $\mathbf{W}_i(t)$, which can be calculated using the fluctuation−dissipation relationship:

$$\langle \mathbf{W}_i(t)\cdot\mathbf{W}_j(t')\rangle = 6k_BT\Gamma\delta_{ij}(t - t') \tag{5}$$

where k_B is the Boltzmann constant, and T is the temperature of the system. Similar to the simulations of the interactions between rigid particles and plasma membranes, constant lateral tension was used in the present work. We used a modified Berendsen barostat to maintain the desired lateral tension. The simulation box and coordinates of beads were rescaled in the dimensions parallel to the membrane (i.e., the x/y dimensions in our simulations) according to the current membrane lateral tension. The scaling factor $\mu_{x/y}$ is given by the following equation:[54]

$$\mu_{x/y} = 1 + \frac{dt}{T_pK}[\Sigma_0 - \Sigma(t)] \tag{6}$$

where dt is the time step, T_p is the relaxation time, K is the compression modulus, Σ_0 is the desired tension, and $\Sigma(t)$ is the current membrane lateral tension:

$$\Sigma(t) = -\frac{P_{xx}(t) + P_{yy}(t)}{2} \tag{7}$$

T_p and K were set to 100 and 0.001, respectively. All of the simulations were run under zero membrane tension (i.e., $\Sigma_0 = 0$).

To calculate the bending energy of membrane (E_b), we used the Helfrich formula:[55]

$$E_b = \int_\eta S\left[\frac{\kappa_m}{2}(C_1 + C_2)^2 + \frac{\kappa_g}{2}(C_1C_2)^2\right]d\eta \tag{8}$$

where κ_m and κ_g are the bending modulus of the mean and Gaussian curvature of the membrane, respectively. S is the area of the particle that has already been engulfed by the membrane. η denotes the wrapping ratio of the nanoparticle, which equals to the ratio of the surface area of BCM is covered by membrane to the entire surface area of BCM ($0 \le \eta \le 1$). This formula has been successfully adopted for calculating the energy barrier for the endocytosis of nanoparticles in existing works.[22,23] In the present work, we used this formula for predicting the energy barrier for completely wrapping a BCM. Although the profiles of E_b as a function of η could be unpredictable, the final value of E_b in the end of endocytosis (i.e., when $\eta = 1$) can be computed. The curvature of membrane wrapping BCM after the endocytosis can be roughly equal to the curvature of spherical BCM. In the present work, the radius of the spherical BCM after endocytosis is approximately 8σ, which implies that the Gaussian curvatures of membrane warping the BCM are $C_1 = C_2 = 1/8\sigma^{-1}$. In addition, the values of κ_m and κ_g were set according to the work performed by Cooke et al.[28] From their results, we set the κ_m and κ_g both to $10\varepsilon_0$.

In the NΣT ensemble (where N, Σ, and T denote the bead number, membrane tension, and system temperature, respectively), all the simulations are carried out in a cubic cell with an initial size of $70 \times 70 \times 70\sigma^3$. The cell has periodical conditions in the x/y directions. A membrane formed from 4400 lipids was set up in the middle of the box, with its surface perpendicular to the z-axis. Half of the lipids were receptors. A micelle self-assembled from amphiphilic diblock copolymers was set up above the plasma membrane initially. Beginning from the initial state shown in Figure 1c, the CGMD simulations were run for at least 5×10^6 dt, where the time step dt was set to 0.01τ (τ is the time unit). The length unit σ and the time unit τ were 1 nm and 0.01 μs, respectively, based on the diffusion constant of the membrane (for details, see Supporting Information, Section 2). This conversion has been used previously in the simulations performed by Shi et al.[15]

RESULTS AND DISCUSSION

We performed simulations to explore BCM−membrane interaction pathways. A micelle self-assembled from 103 $A_{10}B_{10}$ diblock copolymers was used in the first simulation. This value is set according to the preferential micelle aggregation number (the aggregation number distribution profiles of micelles are provided in Supporting Information, Section 1). We varied the binding strength between the B block and the receptors on the membrane (ε_{BR}) from $0.5\varepsilon_0$ to $1.5\varepsilon_0$ to explore possible BCM−membrane interaction pathways. Then, we examined the effect of three important factors on the interaction pathways: the aggregation number of the micelle (N_{agg}), the chain length of the polymer (N_b), and the rigidity of the hydrophobic blocks (k_a). Finally, we analyzed the results and compared them with the existing experimental observations.

BCM−Membrane Interaction Pathways. The simulations were first performed by varying the binding strength between the B block and the receptors on the membrane (ε_{BR}) from $0.5\varepsilon_0$ to $1.5\varepsilon_0$. For smaller ε_{BR}, the BCM could not be internalized and remained outside the membrane. With increasing ε_{BR}, the BCM was wrapped in lipids and taken up by cells. Typical receptor-mediated endocytosis occurred when ε_{BR} was large. This is the main cellular internalization pathway for large particles, and it has been well studied.[4] As ε_{BR} was increased to an extremely large value, the endocytosis pathway

DOI: 10.1021/acs.biomac.6b01674
Biomacromolecules 2017, 18, 797−807

was not observed. The BCM fused into the membrane and became situated between the two layers. According to the final morphologies of the simulations under different values of ε_{BR}, we categorized the BCM−membrane interaction pathways into four types: attachment, semiendocytosis, endocytosis, and fusion. These pathways are illustrated in Figure 2. Figure 2a

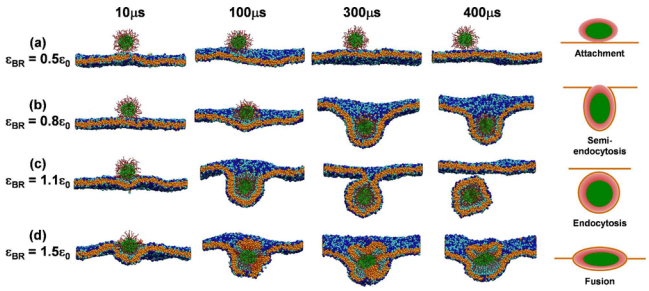

Figure 2. Four pathways of BCM−membrane interaction: (a−d) attachment, semiendocytosis, endocytosis, and fusion, corresponding to ε_{BR} = 0.5, 0.8, 1.1, and $1.5\varepsilon_0$, respectively.

shows snapshots of the attachment pathway. For weak binding between the B blocks and receptors ($\varepsilon_{BR} = 0.5\varepsilon_0$), the BCM cannot be wrapped by lipids, and it remains adhered to the membrane. The process of semiendocytosis for $\varepsilon_{BR} = 0.8\varepsilon_0$ is shown in Figure 2b. After initially contacting the membrane, the BCM is gradually engulfed by the membrane and forms a vesicle wrapped by lipids. However, unlike the traditional endocytosis pathway, in semiendocytosis, the vesicle is connected with the membrane by a "neck" and cannot detach. When ε_{BR} is increased to $1.1\varepsilon_0$, the endocytosis pathway can be observed, as shown in Figure 2c. The BCM is wrapped by lipids and forms a vesicle, which detaches from the membrane. When ε_{BR} was increased further, the BCM was fused into the plasma membrane, as shown in Figure 2d. The morphology shows that the upper layer of bilayer the membrane is ruptured and wraps the BCM when $\varepsilon_{BR} = 1.5\varepsilon_0$. As a consequence, the BCM is set into the membrane and fuses into the two layers. The fusion disrupts the bilayer structure of the plasma membrane, producing pores in the plasma membrane. This could result in leakage of the cytoplasm and the entry of outside molecules, giving rise to cytotoxicity.[2] The schematics of the final morphologies of the four pathways are illustrated in the last column of Figure 2, from which we can clearly see the difference between these pathways.

To obtain comprehensive information about the different BCM−membrane interaction pathways, we calculated the evolutionary wrapping ratio, η, (denoting the engulfment by lipids) and the distance between the BCM and the membrane plane, h, during the interaction process. The results are presented in Figure 3a,b. Figure 3a shows the wrapping ratio of BCM during the four interaction pathways. As shown in the figure, for the attachment pathway, η remains close to 0.3, which means that the BCM is not engulfed by the membrane. For semiendocytosis, η reaches 0.97 at 250 μs, and it remains close to this value after that. This indicates that the BCM can be engulfed by the membrane, but cannot be totally engulfed, due to the "neck" between vesicle and membrane. When endocytosis and fusion occur, η can reach 1.0, denoting complete engulfment of the BCM. In addition, by comparing the wrapping profiles of the last three pathways (i.e., semiendocytosis, endocytosis, and fusion), we find that semiendocytosis and fusion have the slowest and fastest

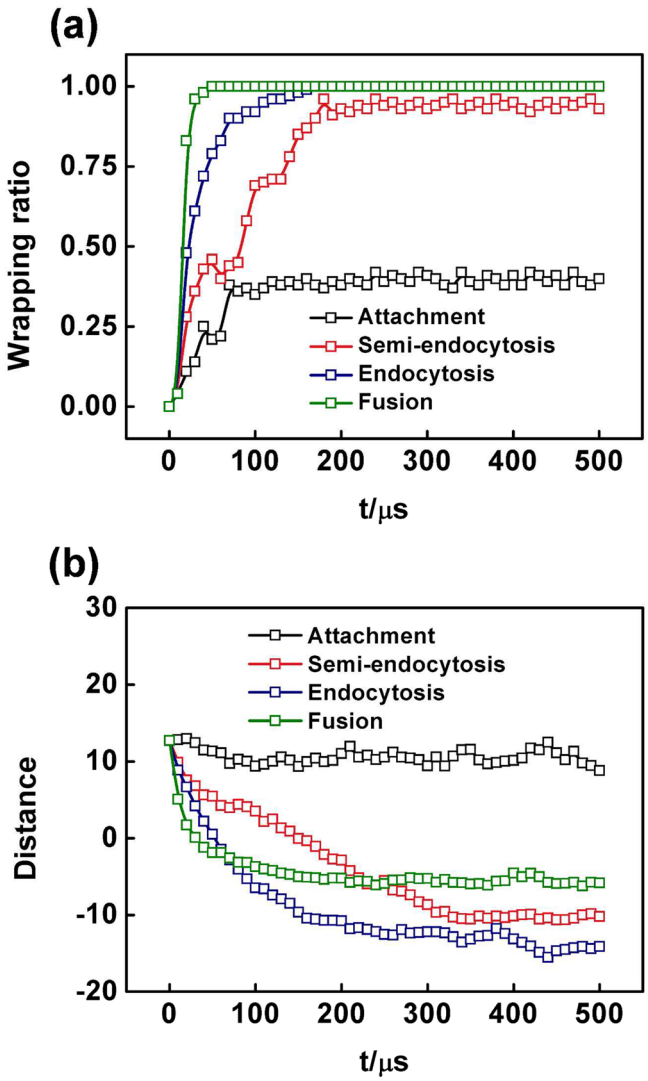

Figure 3. (a) Wrapping ratio of the BCM and (b) the distance between the BCM and the membrane during BCM−membrane interaction.

wrapping rates, respectively. The profiles of the distance between the mass center of BCM and the membrane plane, h, during the four interaction pathways are shown in Figure 3b. The values of h in the attachment pathway are always larger than zero, meaning that the BCM cannot enter the cell. However, for the cases of semiendocytosis and endocytosis, the BCM can go inside the cell. The values of h decrease to nearly −10 *nm* for the two pathways, and this decrease occurs more rapidly for endocytosis than for semiendocytosis. When fusion occurs, the BCM stays inside the bilayer membrane, and h is very close to 0 *nm*, as shown in Figure 3b. The statistical results in Figure 3a,b demonstrate that the endocytosis pathway has the highest cellular uptake capacity.

Unlike rigid particles, BCMs are elastic particles that can change their shapes during BCM−membrane interactions. In this study, we investigated the deformation of BCMs under different interaction pathways. First, the deformation of the BCM core was examined. The attachment pathway was not considered, because this is a rather weak interaction pathway. The aspect ratio $\zeta = r_{xy}/r_z$ was used to characterize the deformations. $\zeta > 1$ and $\zeta < 1$ denote side-oriented (axis in x/y plane is longer) and tip-oriented (axis in z direction is longer)

DOI: 10.1021/acs.biomac.6b01674
Biomacromolecules 2017, 18, 797−807

oblate, respectively. The changes in ζ over time are shown in Figure 4a, and there are illustrations of deformed BCMs under different interaction pathways in Figure 4b. For all three pathways, ζ increased from 1.0 to approximately 1.25 in the beginning, which means that the BCM was deformed from a spherical shape to side-oriented oblate. This deformation increases the contact area between the BCM and the membrane, which can lead to enhanced binding energy between receptors and BCM and improve the BCM–membrane interaction. However, the values of ζ for semi-endocytosis and endocytosis decreased after 80 μs. For the fusion, ζ keeps increasing during the entire interaction process. A decrease in ζ indicates that the BCM has a tendency to deform into a tip-oriented oblate shape. As the engulfment is almost complete, the lipid-wrapped BCM is connected to the membrane via a "neck". A tip-oriented oblate shape may be more favorable for the subsequent breakage of the neck because this shape maintains a smaller contact area between the BCM and the lipids. For the case of endocytosis, ζ decreased to 0.8 at 250τ, which was associated with a tip-oriented oblate shape. In the end, the neck was broken, and the BCM was restored to a spherical shape, as illustrated in the profile that ζ is increased from 0.8 to 1.0. However, the ζ value during semiendocytosis stays below 1.0 because the neck is not broken, and the lipid-wrapped BCM remains stuck to the membrane. Additionally, we examined the morphologies of BCMs after the three types of interactions from different view angles. Our findings about the core shapes of BCMs are well supported by the views from different angles. For details about these morphologies, see Supporting Information, Section 3.

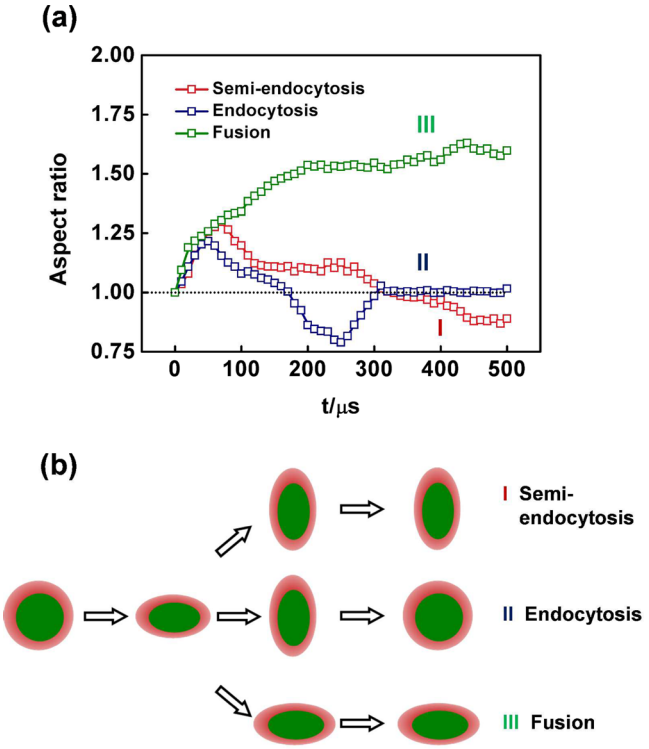

Figure 4. (a) Aspect ratios (the values of r_{xy}/r_z, where r_{xy} and r_z are the average radii in the xy plane and z direction) of the BCM cores (formed by the A block) during the different BCM–membrane interactions. (b) Schematic illustrations of the deformations of the BCM during the interactions. The dashed line in (a) indicates where the aspect ratio equals 1.0, which corresponds to an isotropic spherical shape.

In addition to the BCM core, we examined the deformation of the hydrophilic shell. The representative morphologies of BCM before and after the four types of interactions are provided in Figure 5c–f. Figure 5a shows the profiles of hydrophilic blocks density along the periphery of the BCM as a function of radius angle α, before the interactions begin and after the interactions end. The radius angle α is the angle between the vector along positive z direction normal to the membrane plane and a target vector rotating in the y/z plane. Both the vectors are originated from the mass center of BCM ($0 \le \alpha \le 2\pi$; an illustration of angle α is provided in Figure 5c). Before the BCM–membrane interaction, the density remains nearly constant and independent of α. This means that the hydrophilic blocks are nearly uniformly arranged along the periphery. After the interaction, the distributions of hydrophilic blocks are changed, and the profiles of density differ under different interaction pathways. For semiendocytosis, the density is lower near the "neck" site (where α is close to 0 or 2π). This is because the hydrophilic blocks of the BCM near the membrane are dragged to the receptors on the membrane. The density profile for the fusion shows six peaks and saddles, which correspond to the starfish-like structure of the BCM in Figure 5d. The hydrophilic blocks are stretched into the membrane in six directions in the y/z plane because of their strong binding strength to the receptors on membrane. We had also examined the morphologies of BCMs after fusion under other conditions (e.g., different receptor densities or different binding strength between the hydrophilic blocks and receptors and different polymer chain lengths). The starfish-like structures can always be observed, while the numbers of hydrophilic peaks along the BCM periphery were varied, which could be smaller or larger than six. For the case of endocytosis, the density profile is extremely close to the density value before the BCM–

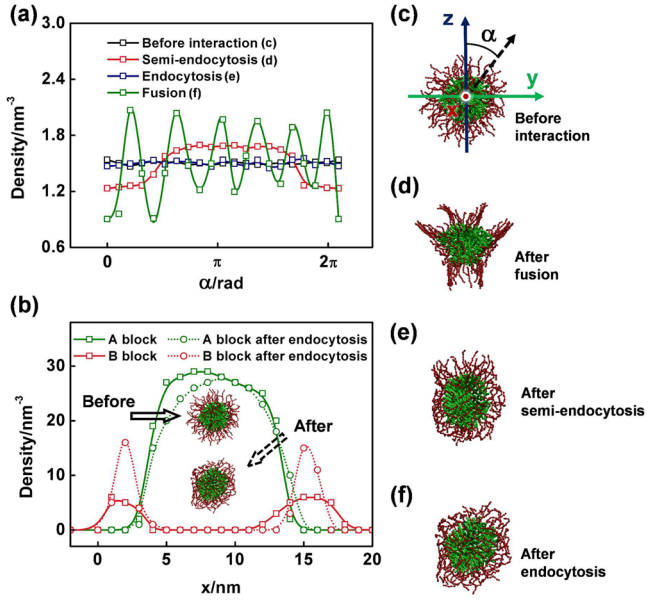

Figure 5. (a) Density of the B block along the circle of the micelle. (b) The densities of the BCM in the radial direction before and after the endocytosis. (c–f) Morphology of the BCM before the interaction and after semiendocytosis, endocytosis, and fusion, respectively. The angle α is a radius angle in y/z plane, as illustrated in (c).

DOI: 10.1021/acs.biomac.6b01674
Biomacromolecules 2017, 18, 797–807

membrane interaction. The hydrophilic blocks are still uniformly packed along the periphery in the shell of BCM after the endocytosis. However, the shell of BCM shrinks after endocytosis, as illustrated in Figure 5f. This figure shows the radial distribution functions (RDF) of BCM before and after endocytosis. The results show that the RDF of hydrophobic blocks remains nearly unchanged after endocytosis. The densities of the hydrophilic blocks increase after endocytosis. These changes indicate that the thickness of the hydrophilic shell decreases after endocytosis, as a consequence of the wrapping of lipids. In addition to the results observed from the positive x direction (front view angle), the morphologies of BCMs after the three types of BCM−membrane interactions from different view angles also validate these foundings. For details about the morphologies of BCMs from different view angles, see Supporting Information, Section 3.

The deformations of BCMs may have a significant effect on the system energy. We further examined the bending energy of the membrane (E_b), the binding energy between the BCM and the membrane (E_{bind}), and the change in the potential energy of the BCM after the interactions (E_{BCM}). The E_b value was calculated from the Helfrich formula (eq 8 in the Model and Methods section). E_b denotes to the energy barrier contributed by the membrane, which has to be overcome by the BCM for a complete endocytosis. In the present work, we assume that the BCM can be endocytosed in every case. And the curvature of membrane wrapping BCM after the endocytosis can be roughly equal to the curvature of BCM, because the BCM after endocytosis maintains an isotropic spherical shape (i.e., $C_1 = C_2 = 1/8\sigma^{-1}$). A similar protocol had been used in the simulation work performed by Li et al.[18] Aside from E_b, which was obtained from theoretical formulations, the other energies were calculated from the CGMD simulation results.

The energy changes as a function of ε_{BR} are shown in Figure 6. As the profiles show, E_b is independent of ε_{BR} and remains constant at $251\varepsilon_0$. With increasing ε_{BR}, E_{bind} increases nonlinearly, exhibiting a faster increase at larger ε_{BR}. This is because of an enlarged contact area between the B blocks and the receptors at larger ε_{BR}. As shown in Figure 5d, the B blocks are bundled and stretched into the membrane in the case of the fusion pathway. Moreover, the conformation of polymer chain changes because of the strong binding between polymer and receptors. The end-to-end distance of the B block increases with increasing ε_{BR} (see Supporting Information, Section 4), which also leads to an increased contact area. The E_{BCM} increases from $10\varepsilon_0$ to $300\varepsilon_0$ with increasing ε_{BR}. Compared with E_b, the E_{BCM} value is extremely small and can be ignored under smaller ε_{BR}. In this case, the attachment and semi-endocytosis pathways occur. However, E_{BCM} is comparable to E_b under larger ε_{BR}, which means that the deformed BCM restores a large amount of energy as the endocytosis and fusion pathways are achieved. In addition, the value of E_{bind} is smaller than that of $E_b + E_{BCM}$ when $\varepsilon_{BR} < 1.1\varepsilon_0$ and larger than $E_b + E_{BCM}$ after $\varepsilon_{BR} \geq 1.1\varepsilon_0$, which indicates that the energy barrier for endocytosis can be overcome when $\varepsilon_{BR} \geq 1.1\varepsilon_0$. This is the reason that BCM cannot be internalized as $\varepsilon_{BR} < 1.1\varepsilon_0$. Thus, the energy analysis can explain the mechanisms of different BCM−membrane interaction pathways. For smaller ε_{BR}, the main barrier is the bending energy of the membrane (E_b), which cannot be overcome, leading to a failure of cellular internalization ($E_{bind} < E_b$). With increasing ε_{BR}, the BCM is deformed during the BCM−membrane interaction process. In this case, both the bending energy of the membrane and the energy restored in the BCM (E_{BCM}) are the main energy barriers. Endocytosis can occur when $E_{bind} > E_b + E_{BCM}$. In our calculations, this can be observed for $\varepsilon_{BR} > 1.1\varepsilon_0$. However, when ε_{BR} is increased further, the extremely high E_{bind} may destroy the uniform alignment of lipids in the bilayer membrane. The BCM is pulled into the membrane, and the fusion pathway occurs as a consequence.

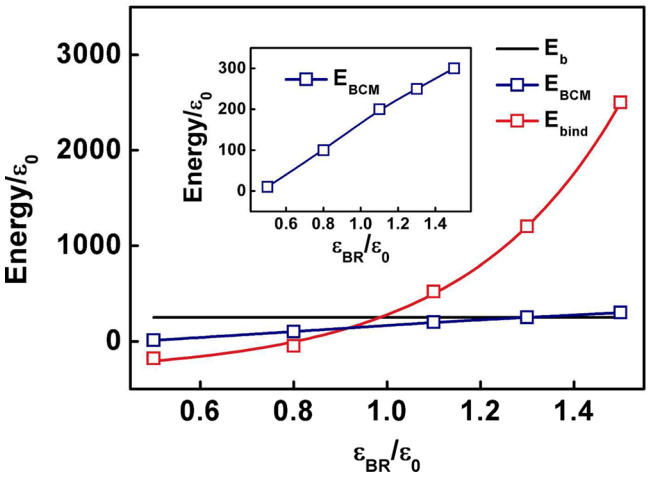

Figure 6. Bending energy of the membrane, the change of the potential energy of the BCM after the interactions, and the binding energy between the BCM and the membrane (denoted by E_b, E_{BCM}, and E_{bind}, respectively) as functions of ε_{BR}. An enlarged view of E_{BCM} is shown in the inset.

Effects of BCM and Diblock Copolymer Structure on the BCM−Membrane Interaction Pathway. *Aggregation Number (N_{agg}) of the BCM.* The self-assembled BCMs have a variety of N_{agg} values, even under the same self-assembly conditions. We studied the effect of N_{agg} on the BCM−membrane interactions. The BCMs were also choses from an additional simulation (Supporting Information, Section 1). In addition to the BCM with $N_{agg} = 103$, two BCMs with $N_{agg} = 54$ and 141 were chosen to perform the CGMD simulations. The number of beads in the A and B blocks were both set to 10 (i.e., $A_{10}B_{10}$). For each BCM, the simulations were run under different values of ε_{BR}, from $0.5\varepsilon_0$ to $1.5\varepsilon_0$.

On the basis of the simulation results, we found that the internalization capacities of BCMs vary with changes in N_{agg}. The representative snapshots from the ends of simulations are shown in Figure 7a, in which $\varepsilon_{BR} = 1.0$, 1.1, and $1.3\varepsilon_0$. When N_{agg} is small ($N_{agg} = 54$), the BCM can only be semi-endocytosed by the membrane for $\varepsilon_{BR} \geq 1.0\varepsilon_0$. As N_{agg} is increased to 103, complete endocytosis can be observed when $\varepsilon_{BR} = 1.1\varepsilon_0$, but the endocytosis cannot be accomplished under smaller ε_{BR}. The fusion pathway can occur when ε_{BR} is increased to $1.3\varepsilon_0$. As N_{agg} is increased to 141, a greater capacity for endocytosis is observed because the BCM can be endocytosed under smaller ε_{BR} ($\varepsilon_{BR} = 1.0\varepsilon_0$). The fusion pathway is obtained when $\varepsilon_{BR} \geq 1.1\varepsilon_0$. The results indicate that, with increasing N_{agg}, the cell internalization capacity of the BCM increases. However, if the BCM has an N_{agg} that is too large, it can lead to a facile fusion pathway, in which the bilayer structure of the membrane is disrupted. Cytotoxicity is produced as a consequence. These results provide guidance for the design of BCMs as a DDS. The N_{agg} should be carefully considered and engineered to obtain more efficient cellular uptake and lower cytotoxicity.

DOI: 10.1021/acs.biomac.6b01674
Biomacromolecules 2017, 18, 797−807

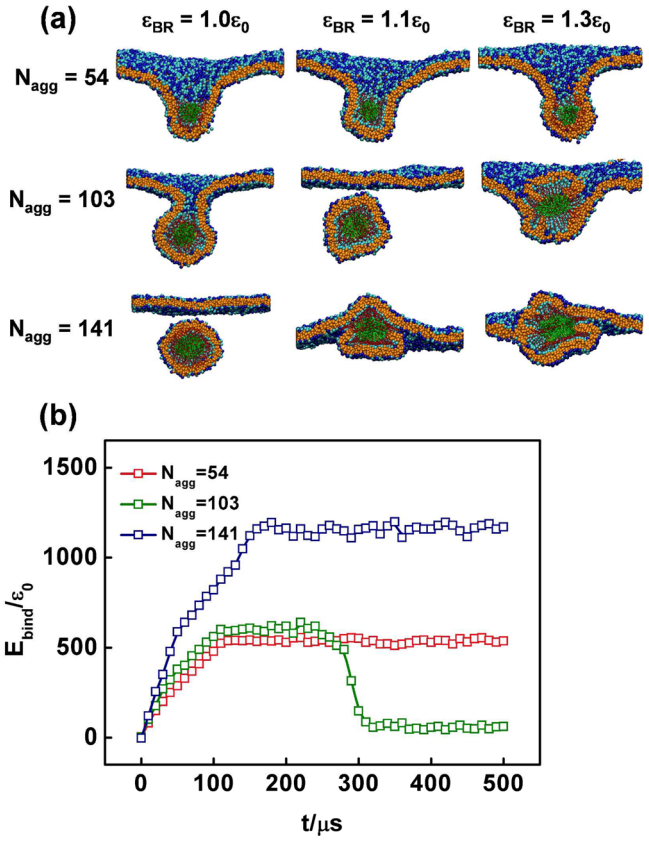

Figure 7. (a) Snapshots of the systems at the end of the BCM–membrane interactions for BCMs with different aggregation numbers (N_{agg}) at different ε_{BR}. (b) The E_{bind} values during the interaction procedures for the BCMs with various N_{agg} at $\varepsilon_{BR} = 1.1\varepsilon_0$.

Representative snapshots from the ends of simulations are shown in Figure 8a. For smaller N_b (N_b = 12, i.e., A_6B_6),

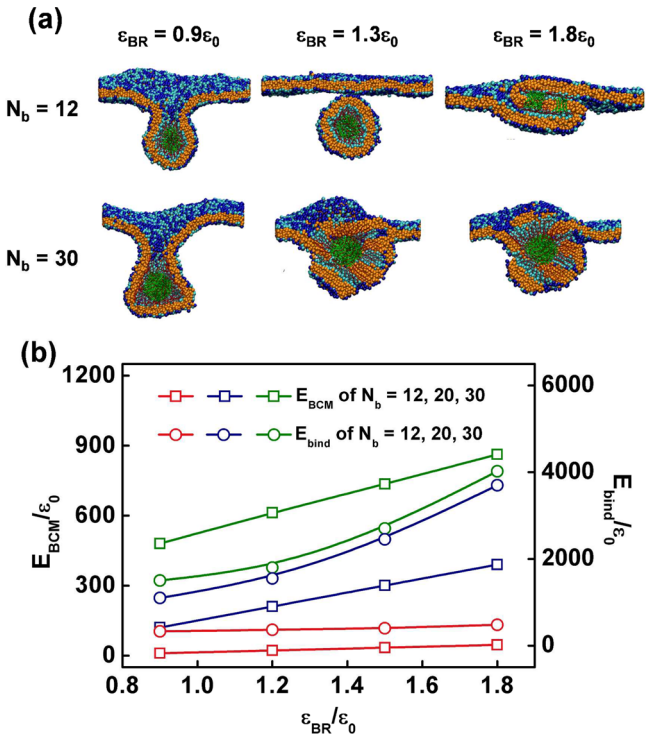

Figure 8. (a) Snapshots of the systems at the end of the BCM–membrane interactions for BCMs with different chain lengths of polymers (N_b) at various values of ε_{BR}. (b) The E_{BCM} and E_{bind} values as functions of ε_{BR} for the BCMs with N_b = 12, 20, and 30.

The different BCM–membrane interactions under a variety of N_{agg} values are mainly dependent on the different binding strengths between the BCM and the membrane. We calculated E_{bind} during the interaction procedures at N_{agg} = 64, 103, and 141. The statistical results are shown in Figure 7b. The E_{bind} values increase before 250 μs for all three N_{agg} values. However, the increase is faster for larger N_{agg} because more B blocks are binded to the receptors in this case. For N_{agg} = 141, the extreme binding energy destroys the original ordered packing of the lipids, leaving more spaces into which the polymers can be easily stretched. Therefore, the BCMs with larger N_{agg} exhibit a greater capacity to fuse into the membrane. In addition, the E_{bind} for N_{agg} = 103 decreases rapidly to almost zero after 250 μs. This can be attributed to the detachment of the BCM wrapped by lipids, which occurs when the endocytosis is finished. As the BCM is completely engulfed by lipids, there is no driving force for the BCM–membrane interaction.

Chain Length of Polymers (N_b). In addition to the aggregation number, the chain length of the polymer is significant for the BCM. We performed simulations to examine the effect of chain length on the BCM–membrane interactions. The chain length was regulated by varying the number of beads in each polymer chain, denoted by N_b. Two cases were considered, N_b = 12 and 30, in which the numbers of beads in both blocks were set to 6 or 15 (i.e., A_6B_6 and $A_{15}B_{15}$). The aggregation number of the BCM, N_{agg}, was set to 103 in both cases. Simulations were run with ε_{BR} ranging from $0.9\varepsilon_0$ to $1.8\varepsilon_0$.

semiendocytosis, endocytosis, and fusion can be observed, which is similar to the results when N_b = 20 (i.e., $A_{10}B_{10}$). Meanwhile, a degradation of the micelle can be observed in the fusion pathway. As shown in the figure, when $\varepsilon_{BR} = 1.8\varepsilon_0$, the core of the micelle formed by A_6B_6 is separated into seveal parts. This degradation phenomenon dose not occur for the micelles with N_b = 20 or 30. This is because the cores of micelles with N_b = 20 and 30 are more frozen than those with N_b = 16, which is due to more attractive interaction between solvophobic units resulted from increased length of solvophobic blocks. The critical binding strength for endocytosis and fusion are both higher than for N_b = 20. For larger N_b ($A_{15}B_{15}$), the semiendocytosis and fusion pathways were obtained, but endocytosis was not observed at any ε_{BR}, indicating a reduced cellular uptake capacity. In addition, larger N_b may lead to higher cytotoxicity because fusion occurs even under smaller ε_{BR}. Therefore, similar to the aggregation number of BCM, the N_b of polymers should also be designed to obtain good cellular internalization performance and low cytotoxicity. We also examined the effect of A/B block volume fractions ($A_{16}B_4$ and A_4B_{16}, N_{agg} for both BCMs were set to 103) on the BCM–membrane interactions. Lower endocytosis capacity were observed for both $A_{16}B_4$ and A_4B_{16}, and higher cytotoxicity was found for A_4B_{16}. Therefore, an equivalent hydrophobic/hydrophilic block volume fraction can contribute to increasing the cellular uptake capacity. Details about the effect of the A/B block volume fraction can be found in the Supporting Information, Section 5.

DOI: 10.1021/acs.biomac.6b01674
Biomacromolecules 2017, 18, 797–807

To understand the mechanisms underlying the N_b-dependent internalization performance of the BCM, we further investigated the energy of the BCM−membrane interaction system under different values of N_b. E_{BCM} and the E_{bind} as functions of ε_{BR} are shown in Figure 8b. Both E_{BCM} and E_{bind} increase with increasing ε_{BR}. At lower N_b, the E_{BCM} is extremely small. The deformation of BCM has a weak effect on the interaction pathways. E_{bind} is higher than E_{BCM}, indicating that the BCM−membrane binding energy may overcome the energy barrier of E_{BCM}, which makes endocytosis possible. However, when N_b is increased to 20, E_{BCM} is much higher than E_{bind}. The deformed BCM restores high energy, consuming the energy that gives rise to a weakened internalization capacity. In addition, the high BCM−membrane binding strength makes the hydrophilic blocks stretch into the bilayer membrane, producing higher cytotoxicity.

Rigidity of the Hydrophobic Blocks. In addition to coil−coil diblock copolymers, rod−coil copolymers can form micelles. The chain stiffness may result in unique BCM−membrane interaction performance. We performed the simulation under various rigidities of the A block. A harmonic spring potential was applied between the first and third beads of a three-body angle. The formula for this potential is given in eq 2. The chain stiffness is regulated by changing the strength k_a from 0 to $5\varepsilon_0/\sigma^2$. A larger k_a corresponds to stronger chain stiffness. The ε_{BR} is set to $1.1\varepsilon_0$. All the BCMs were formed by 103 $A_{10}B_{10}$ copolymers.

First, we calculated the persistence length (l_p) as a function of k_a. The l_p value can directly represent the chain stiffness. The formula for l_p is as follows:[56]

$$\langle \cos(\theta_i) \rangle = \exp(-il_b/l_p) \tag{9}$$

θ_i is the angle between two neighboring bonds along the chain. l_b is the average length of all the i bonds. The profile of l_p as a function of k_a is shown in the inset of Figure 9. There is a slight increase in l_p for $k_a < 2\varepsilon_0/\sigma^2$. The increase is much faster for the case of $k_a > 2\varepsilon_0/\sigma^2$. Consequently, weak and strong chain stiffness are observed for $0\varepsilon_0/\sigma^2 < k_a < 2\varepsilon_0/\sigma^2$ and $k_a > 2\varepsilon_0/\sigma^2$, respectively. We next studied the BCM−membrane interaction pathways under three different chain stiffness levels: $k_a = 0\varepsilon_0/\sigma^2$ (flexible), $1\varepsilon_0/\sigma^2$ (weak stiffness), and $5\varepsilon_0/\sigma^2$ (strong stiffness).

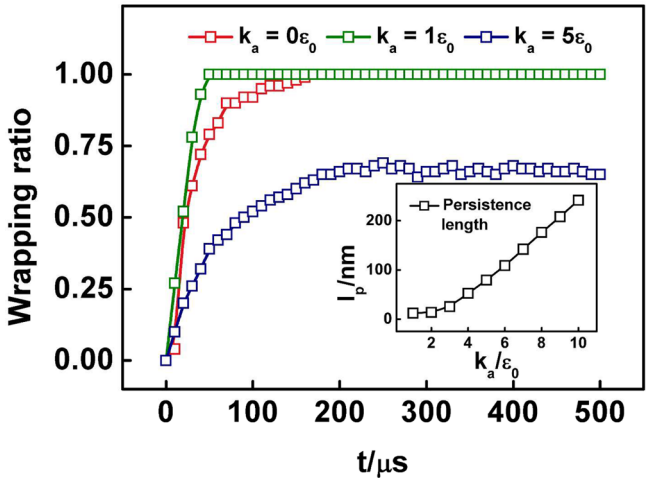

Figure 9. Wrapping ratios of the BCMs with different rigidities of the A blocks during the BCM−membrane interactions. The inset illustrates the persistence length of the A blocks as a function of k_a.

The wrapping ratio as a function of time for the BCM under the three chain stiffnesses is shown in Figure 9. For flexible and weak stiffness, the endocytosis pathway is observed. As shown in the figure, the wrapping ratio can be increased to 1.0 when the chain stiffness equals $0\varepsilon_0/\sigma^2$ or $1\varepsilon_0/\sigma^2$, but the increase in the wrapping ratio is faster for $k_a = 1\varepsilon_0/\sigma^2$ than for $k_a = 0\varepsilon_0/\sigma^2$. Therefore, the BCMs self-assembled from the rod−coil diblock copolymers have greater cellular internalization capacity than the coil−coil diblock copolymers. However, when the chain stiffness is increased to $5\varepsilon_0/\sigma^2$, the BCM cannot be completely engulfed by lipids, and semiendocytosis occurs. Thus, a stronger chain stiffness results in a weakened cellular uptake capacity, and a weak chain stiffness is better for obtaining BCMs with high cellular internalization efficacies.

These different internalization capacities can be attributed to the relatively stable spherical and nonspherical BCM shapes under weak and strong chain stiffness, respectively. For the BCMs self-assembled from flexible polymers ($k_a = 0\varepsilon_0/\sigma^2$), their shapes can be greatly changed during the BCM−membrane interaction, restoring a large amount of energy and leading to reduced cellular uptake efficacy. When rigidity is introduced to the chain ($k_a = 1\varepsilon_0/\sigma^2$), the deformation can be weakened due to the relatively rigid BCM structure. The restored energy is reduced, and the cellular internalization efficacy consequently increases. However, as the chain stiffness is increased further ($k_a = 5\varepsilon_0/\sigma^2$), the BCM favors a polyhedron morphology during the BCM−membrane interaction. Compared to the spherical BCM that occurs when the rod blocks have lower k_a, the polyhedral BCM has a larger surface area per unit volume, which increases the energy for engulfing the BCM.[57] Thus, a strong chain stiffness of the polymers is not beneficial for endocytosis.

Comparison with Experimental Observations. This study has shown that the structure of a polymer strongly affects the BCM−membrane interaction processes. Some experimental evidence are available in the literatures, supporting the theoretical results. For example, Lavasanifar et al. studied the effect of block copolymer structures of poly(ε-caprolactone)-*b*-poly(ethylene oxide) (PCL-*b*-PEO) on the cellular internalization of BCMs formed by these polymers.[46] Comparing the in vitro results under various molecular weights (M_w of PCL = 5000, 13 000, and 24 000 g/mol and M_w of PEO = 2000, 5000, and 13 000 g/mol), they found superior cellular internalization of the micelles formed from polymers with M_w of PCL = 13000 or PEO = 5000 (medium molecular weight). They also confirmed that the major cellular internalization pathway of the BCMs is clathrin-mediated endocytosis. The profiles of cellular uptake percentage are reproduced in Figure 10a. As can be seen, for the lowest (PEO_{2000}) and highest (PCL_{24000} and PEO_{13000}) molecular weight, the BCMs exhibit poor cellular uptake performances. For the case of PEO_{13000}, the uptake percentage is extremely low, which is approximately 0.5%. While, for PEO_{5000} and PCL_{13000}, a relative higher uptake percentage can be observed.

Herein, we performed additional simulations to study the cellular uptake percentage of the BCMs formed by PCL-*b*-PEO with different chain lengths. The PCL and PEO blocks can be viewed as corresponding to the hydrophobic (A) and hydrophilic (B) segments, respectively, in our simulations. Because PCL and PEO have similar monomer structures (alkane backbones with oxygen), their molecular weights can be roughly associated with the chain length of the polymers. For the sake of computations, one coarse-grained bead in the

DOI: 10.1021/acs.biomac.6b01674
Biomacromolecules 2017, 18, 797−807

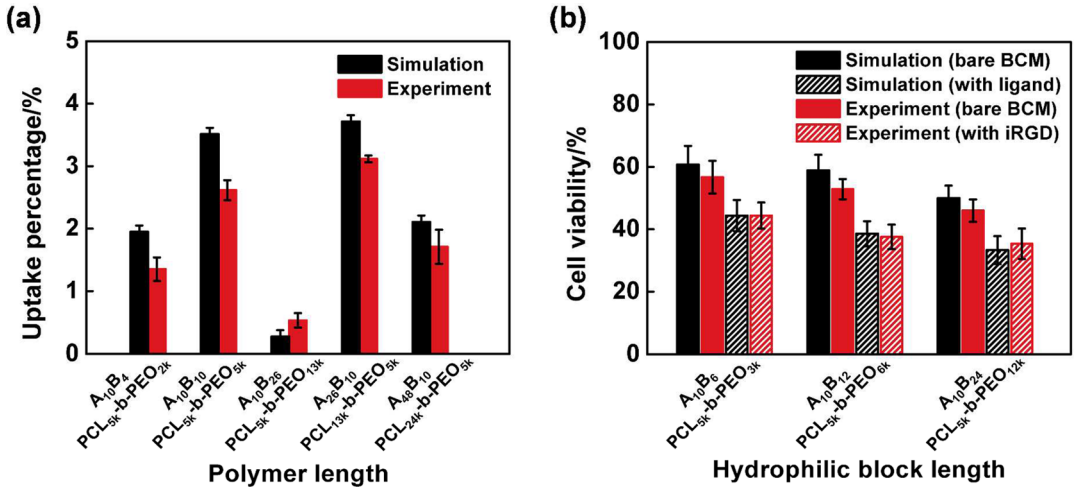

Figure 10. (a) Cellular uptake percentage of BCMs formed by different polymer lengths from the present simulations and exsisting experiments performed by Lavasanifar et al.[46] (b) Cell viability after incubated with BCMs formed by polymers with various hydrophilic block lengths from our simulations and the experimental results obtained by Zhu et al.[47]

polymer model represents 500 g/mol molecular weight (about 12 $C_2H_2C_2H_2O$ unit). Therefore, the $PCL_{5000/13000/24000}$-*b*-$PEO_{2000/5000/13000}$ are denoted by $A_{10/26/48}B_{4/10/26}$ in the simulations. Details about the simulation system and parameter setting can be found in Supporting Information, Section 6. According to the simulated results, we calculated the cellular uptake percentage. In the calculation, a complete endocytosis was regarded as a successful cellular uptake. The statistical results are provided in Figure 10a. A predominant cellular uptake performance can be seen for $A_{10}B_{10}$ and $A_{26}B_{10}$. The $A_{10}B_{26}$ exhibits the lowest uptake percentage, which is about 0.28%. As a result, the BCMs exhibit the highest cellular uptake performance when the block copolymers have medium chain lengths. It should be noted that, due to the limitation of current computational ability, theoretical simulations cannot obtain statistical results exactly the same with those in experiments.[15,18,37] Meanwhile, these results are qualitatively consistent with the experimental observations. Both the experiment and simulation showed that a medium polymer length gives higher cellular uptake, and micelles with shorter or longer polymers are not suitable for obtaining desirable internalization performance. Accordingly, these experimental results are theoretically supported by our simulations.

Additionally, although Lavasanifar et al. successfully found that micelles formed from medium-length polymers have higher cellular internalization capacities, the mechanisms underlying this finding remain unclear. From the simulations, we learned that the main reason for the lower endocytosis capacity of the micelles with shorter polymers is the reduced binding strength between the BCM and the membrane. This reduced binding strength cannot overcome the bending energy barrier of the membrane, which is required for completing endocytosis. Thus, in this case, attachment or semiendocytosis occurs. For the micelles with longer polymer chains, the binding energy between the BCM and membrane is higher. The BCM does not tend to enter the cell; instead, it fuses into the membrane. This results in reduced cellular uptake.

In addition, our simulation confirmed the phenomenon that the cytotoxicity of BCM is regulated by the polymer length, which had been observed via experimental approaches. Recently, Zhu et al. explored the drug-delivery performance of poly(ε-caprolactone)-*b*-poly(*N*-vinylpyrrolidone) (PCL-*b*-PVP) micelles with different lengths of PVP (hydrophilic) blocks.[47] Three different PVP molecular weights were studied: 3000, 6000, and 12 000 (M_n). By examining the H22 cell viability after incubating with different BCM concentrations, it was found that, for bare BCMs, the cytotoxicity is independent of the PVP length. When an iRGD targeting moiety was conjugated to the BCM, the cytotoxicity of the BCMs increased. Moreover, longer PVP lengths may results in higher cytotoxicity at some micelle concentrations. For clarity, we represent their results in Figure 10b. It can be seen that the cell viability for the BCMs conjugated with iRGD is much smaller than the bare ones. Moreover, with an increase in the molecular weight of the PVP block, the cell viability is gradually decreased, corresponding to the increase of cytotoxicity.

Similar to the above example, we performed simulations on the cytotoxicity of BCMs formed by the amphiphilic block copolymers with different length of hydrophilic blocks. The PCL and PVP blocks can be viewed as corresponding to the A (hydrophobic) and B (hydrophilic) blocks, respectively, in our simulations. Again, the chain lengths of polymers in the simulation are proportional to the molecular weight of PCL-*b*-PVP, and one coarse-grained bead in the polymer model corresponds to 500 g/mol molecular weight. As a result, the PCL_{5000} and $PVP_{3000/6000/12000}$ is denoted by A_{10} and $B_{6/12/24}$ in the simulations, respectively. Weak binding strength between the BCM and the membrane in the simulations (i.e., $\varepsilon_{BR} = 1.1k_BT$) correspond to the case of bare BCMs. In order to simulate the case of BCMs conjugated with iRGD, we used a larger binding strength between the last beads of hydrophilic blocks. Herein we set ε_{LR} to $4.0k_BT$, this value had been widely used in the simulations regarding the ligand−receptor binding in existing works,[22,50] which can effectively denote the actual binding strength between ligand and receptor. For details about the simulation, see Supporting Information, Section 6. According to previous experiment and simulation,[57−59] the disruption of lipids in the plasma membrane is primarily responsible for the cytotoxicity during the particle−membrane interactions because it leads to the leakage of the cytoplasm and the entry of outside molecules. These phenomena have also been found in the fusion pathway in the present simulations. Therefore, the fusion of BCMs is regarded as the main reason for the cytotoxicity in the BCM−membrane interactions. Figure

DOI: 10.1021/acs.biomac.6b01674
Biomacromolecules 2017, 18, 797−807

10b shows the statistical results from simulations. The cell viability for bare BCM is higher than that for the BCM with iRGD, and the cell viability is reduced with increasing the length of B block. Therefore, BCMs with longer polymer chains may lead to higher cytotoxicity at stronger binding strength between the BCM and the membrane. Our analysis further reveals that this result is mainly caused by the higher energy at longer hydrophilic block lengths at larger binding strength between membrane and hydrophilic blocks of BCM, which is responsible for the damage to the bilayer membrane (Figure 8b). Regarding the polymer-length-regulated cytotoxicity phenomenon, the simulations find good agreement with the existing experimental observations and provide a theoretical understanding of the experimental findings.

The above comparisons indicate that, by setting the certain parameters in our simulations according to those in the experiments (e.g., hydrophobic/hydrophilic volume fraction, the binding strength between the hydrophilic blocks/ligand moieties and the receptors on the membrane), a qualitatively consistence between the simulated results and experimental observations can be obtained. In addition, we have examined the effect of these uncertain parameters on the final results. For example, we performed the simulations by varying the receptor density (from 0.5 to 0.1). The results indicated that, for all the cases, the cellular uptake percentages are synchronously reduced and the cell viabilities are synchronously increased compared to those when the receptor density is 0.5. Meanwhile, the qualitatively consistence between simulated results and experimental results remained.

The experiments have only examined the effects of certain parameters (e.g., polymer length and hydrophobic/hydrophilic volume fraction) on the cellular internalization of BCMs. Our simulations were able to examine the effects of various parameters of the BCM and polymer (e.g., aggregation number of BCM and the chain stiffness of hydrophobic blocks) on the BCM−membrane interactions. We not only obtained results that were qualitatively consistent with those obtained from experiments but also predicted the relationships between cellular internalization and several important structural parameters of the BCM and the polymer. Moreover, the mechanisms underlying the BCM/polymer effects on the interaction pathways were revealed. As BCMs have been used for high-efficiency drug-delivery systems (DDSs), these simulation results could be helpful for designing improved DDSs with better cellular uptake performance and lower cytotoxicity, which would be beneficial for applications such as tumor therapy.

CONCLUSIONS

Using coarse-grained molecular dynamic simulations, we investigated the interaction pathways between block copolymer micelles (BCM) and plasma membranes. Four pathways were discovered: attachment, semiendocytosis, endocytosis, and fusion. Endocytosis was the most efficient pathway for the uptake of BCMs, and fusion can result in cytotoxicity. The deformation of the BCM during the interaction not only affects the binding energy between the BCM and the membrane, it also increases the energy barrier for internalization, which significantly affects the interaction pathways. By examining the effect of the aggregation number of the BCM (N_{agg}), the chain length of polymers (N_b), and the chain stiffness of the hydrophobic block (k_a) on the BCM−membrane interactions, we learned that a smaller N_{agg} and lower N_b can lead to weaker cellular uptake capacity of the BCM, whereas a larger N_{agg} and higher N_b produce higher cytotoxicity. Moreover, lower chain stiffness in the hydrophobic block could be favorable for obtaining BCMs with higher internalization efficacy and lower cytotoxicity. The changes in cellular uptake performance based on polymer structure are in qualitative agreement with the existing experimental observations. In addition, the mechanisms underlying the polymer BCM−membrane interaction pathways, which are difficult to study via experimental approaches, were revealed in the present work. The findings could provide guidance for designing BCMs to be used as drug-delivery systems with higher therapeutic efficacy and lower side effects/toxicity to the human body.

ASSOCIATED CONTENT

Supporting Information

The Supporting Information is available free of charge on the ACS Publications website at DOI: 10.1021/acs.biomac.6b01674.

Self-assembly of block copolymer micelles, unit conversion, morphologies of BCMs after the BCM−membrane interactions from different view angles, end-to-end distance of the polymer, effect of the A/B volume fraction, parameter setting in the comparison with experimental observations (PDF)

AUTHOR INFORMATION

Corresponding Authors

*E-mail: jlin@ecust.edu.cn. Tel: +86-21-6425-3370.
*E-mail: lq_wang@ecust.edu.cn.

ORCID

Jiaping Lin: 0000-0001-9633-4483

Notes

The authors declare no competing financial interest.

ACKNOWLEDGMENTS

This work was supported by the National Natural Science Foundation of China (51303055, 21234002, and 21474029). Support from Project of Shanghai Municipality (16520721900 and 14DZ2261205) is also appreciated.

REFERENCES

(1) Sun, T.; Zhang, Y. S.; Pang, B.; Hyun, D. C.; Yang, M.; Xia, Y. *Angew. Chem., Int. Ed.* **2014**, *53* (46), 12320−12364.
(2) Ding, H.; Ma, Y. *Small* **2015**, *11* (9−10), 1055−1071.
(3) Bahrami, A. H.; Raatz, M.; Agudo-Canalejo, J.; Michel, R.; Curtis, E. M.; Hall, C. K.; Gradzielski, M.; Lipowsky, R.; Weikl, T. R. *Adv. Colloid Interface Sci.* **2014**, *208* (24), 214−224.
(4) Sahay, G.; Alakhova, D. Y.; Kabanov, A. V. *J. Controlled Release* **2010**, *145* (3), 182−195.
(5) Kim, S.; Shi, Y.; Kim, J. Y.; Park, K.; Cheng, J.-X. *Expert Opin. Drug Delivery* **2010**, *7* (1), 49−62.
(6) Pippa, N.; Pispas, S.; Demetzos, C. *Curr. Pharm. Des.* **2016**, *22* (19), 2788−2795.
(7) Mikhail, A. S.; Allen, C. *J. Controlled Release* **2009**, *138* (3), 214−223.
(8) Lin, J.; Zhu, J.; Chen, T.; Lin, S.; Cai, C.; Zhang, L.; Zhuang, Y.; Wang, X.-S. *Biomaterials* **2009**, *30* (1), 108−117.
(9) Wei, L.; Cai, C.; Lin, J.; Chen, T. *Biomaterials* **2009**, *30* (13), 2606−2613.
(10) Jiang, R.; Jin, Q.; Li, B.; Ding, D.; Shi, A.-C. *Macromolecules* **2006**, *39* (17), 5891−5896.

DOI: 10.1021/acs.biomac.6b01674
Biomacromolecules 2017, 18, 797−807

(11) Glebov, O. O.; Bright, N. A.; Nichols, B. J. *Nat. Cell Biol.* **2006**, *8* (1), 46−54.
(12) Sahay, G.; Kim, J. O.; Kabanov, A. V.; Bronich, T. K. *Biomaterials* **2010**, *31* (5), 923−933.
(13) Ruan, G.; Agrawal, A.; Marcus, A. I.; Nie, S. M. *J. Am. Chem. Soc.* **2007**, *129* (47), 14759−14766.
(14) Ding, H.; Ma, Y. *Biomaterials* **2014**, *35* (30), 8703−8710.
(15) Shi, X.; von dem Bussche, A.; Hurt, R. H.; Kane, A. B.; Gao, H. *Nat. Nanotechnol.* **2011**, *6* (11), 714−719.
(16) Bahrami, A. H. *Soft Matter* **2013**, *9* (36), 8642−8646.
(17) Yue, T.; Zhang, X. *ACS Nano* **2012**, *6* (4), 3196−3205.
(18) Li, Y.; Kröger, M.; Liu, W. K. *Biomaterials* **2014**, *35* (30), 8467−8478.
(19) Baumgärtner, A.; Skolnick, J. *Phys. Rev. Lett.* **1995**, *74* (11), 2142−2145.
(20) Pogodin, S.; Werner, M.; Sommer, J.-U.; Baulin, V. A. *ACS Nano* **2012**, *6* (12), 10555−10561.
(21) Bemporad, D.; Luttmann, C.; Essex, J. W. *Biophys. J.* **2004**, *87* (1), 1−13.
(22) Vácha, R.; Martinez-Veracoechea, F. J.; Frenkel, D. *Nano Lett.* **2011**, *11* (12), 5391−5395.
(23) Huang, C.; Zhang, Y.; Yuan, H.; Gao, H.; Zhang, S. *Nano Lett.* **2013**, *13* (9), 4546−4550.
(24) Gratton, S. E. A.; Ropp, P. A.; Pohlhaus, P. D.; Luft, J. C.; Madden, V. J.; Napier, M. E.; DeSimone, J. M. *Proc. Natl. Acad. Sci. U. S. A.* **2008**, *105* (33), 11613−11618.
(25) Ding, H.; Ma, Y. *Nanoscale* **2012**, *4* (12), 1116−1122.
(26) Gao, H.; Shi, W.; Freund, L. B. *Proc. Natl. Acad. Sci. U. S. A.* **2005**, *102* (77), 9469−9474.
(27) Mao, J.; Chen, P.; Liang, J.; Guo, R.; Yan, L. T. *ACS Nano* **2016**, *10* (1), 1493−1502.
(28) Cooke, I. R.; Deserno, M. *J. Chem. Phys.* **2005**, *123* (22), 224710.
(29) Sun, J.; Zhang, L.; Wang, J.; Feng, Q.; Liu, D.; Yin, Q.; Xu, D.; Wei, Y.; Ding, B.; Shi, X.; Jiang, X. *Adv. Mater.* **2015**, *27* (8), 1402−1407.
(30) Hu, X.; Hu, J.; Tian, J.; Ge, Z.; Zhang, G.; Luo, K.; Liu, S. *J. Am. Chem. Soc.* **2013**, *135* (46), 17617−17629.
(31) Liang, J.; Chen, P.; Dong, B.; Huang, Z.; Zhao, K.; Yan, L. T. *Biomacromolecules* **2016**, *17* (5), 1834−1844.
(32) Yan, L. T.; Yu, X. *Macromolecules* **2009**, *42* (16), 6277−6283.
(33) Yue, T.; Zhang, X. *Soft Matter* **2013**, *9* (2), 559−569.
(34) Yi, X.; Gao, H. *Phys. Rev. E* **2014**, *89* (6), 062712.
(35) Xie, L.; Tian, W.; Ma, Y. *Soft Matter* **2013**, *9* (39), 9319−9325.
(36) Allen, C.; Maysinger, D.; Eisenberg, A. *Colloids Surf., B* **1999**, *16* (1−4), 3−27.
(37) Chen, L.; Jiang, T.; Cai, C.; Wang, L.; Lin, J.; Cao, X. *Adv. Healthcare Mater.* **2014**, *3* (9), 1508−1517.
(38) York, A. W.; Kirkland, S. E.; McCormick, C. L. *Adv. Drug Delivery Rev.* **2008**, *60* (9), 1018−1036.
(39) Nagasaki, Y.; Yasugi, K.; Yamamoto, Y.; Harada, A.; Kataoka, K. *Biomacromolecules* **2001**, *2* (4), 1067−1070.
(40) Li, X.; Qian, Y.; Liu, T.; Hu, X.; Zhang, G.; You, Y.; Liu, S. *Biomaterials* **2011**, *32* (27), 6595−6605.
(41) Zhu, Z.; Li, Y.; Li, X.; Li, R.; Jia, Z.; Liu, B.; Guo, W.; Wu, W.; Jiang, X. *J. Controlled Release* **2010**, *142* (3), 438−446.
(42) Lee, H.; Hu, M.; Reilly, R. M.; Allen, C. *Mol. Pharmaceutics* **2007**, *4* (5), 769−781.
(43) Luo, L.; Tam, J.; Maysinger, D.; Eisenberg, A. *Bioconjugate Chem.* **2002**, *13* (6), 1259−1265.
(44) Rapoport, N.; Marin, A.; Luo, Y.; Prestwich, G. D.; Muniruzzaman, M. D. *J. Pharm. Sci.* **2002**, *91* (1), 157−170.
(45) Miyata, K.; Oba, M.; Kano, M. R.; Fukushima, S.; Vachutinsky, Y.; Han, M.; Koyama, H.; Miyazono, K.; Nishiyama, N.; Kataoka, K. *Pharm. Res.* **2008**, *25* (12), 2924−2936.
(46) Mahmud, A.; Lavasanifar, A. *Colloids Surf., B* **2005**, *45* (2), 82−89.
(47) Zhu, Z.; Xie, C.; Liu, Q.; Zhen, X.; Zheng, X.; Wu, W.; Li, R.; Ding, Y.; Jiang, X.; Liu, B. *Biomaterials* **2011**, *32* (35), 9525−9535.
(48) Peng, K.-Y.; Wang, S.-W.; Lee, R.-S. *J. Polym. Sci., Part A: Polym. Chem.* **2013**, *51* (13), 2769−2781.
(49) Hsu, H.; Sen, S.; Pearson, R. M.; Uddin, S.; Král, P.; Hong, S. *Macromolecules* **2014**, *47* (19), 6911−6918.
(50) Schubertová, V.; Martinez-Veracoechea, F. J.; Vácha, R. *Soft Matter* **2015**, *11* (14), 2726−2730.
(51) Zhang, L.; Feng, Q.; Wang, J.; Zhang, S.; Ding, B.; Wei, Y.; Dong, M.; Ryu, J.-Y.; Yoon, T.-Y.; Shi, X.; Sun, J.; Jiang, X. *ACS Nano* **2015**, *9* (10), 9912−9921.
(52) Schneider, T.; Stoll, E. *Phys. Rev. B: Condens. Matter Mater. Phys.* **1978**, *17* (3), 1302−1322.
(53) Grest, G. S.; Kremer, K. *Phys. Rev. A: At., Mol., Opt. Phys.* **1986**, *33* (5), 3628−3631.
(54) Berendsen, H. J. C.; Postma, J. P. M.; van Gunsteren, W. F.; DiNola, A.; Haak, J. R. *J. Chem. Phys.* **1984**, *81* (8), 3684−3690.
(55) Helfrich, W. *Z. Naturforsch C* **1973**, *28* (11), 693−703.
(56) Doi, M.; Edwards, S. F. *The Theory of Polymer Dynamics*; Oxford University Press: Oxford, 1986.
(57) Liu, Y.; Tan, J.; Thomas, A.; Ou-Yang, D.; Muzykantov, V. R. *Ther. Delivery* **2012**, *3* (2), 181−194.
(58) Li, Y.; Zhang, X.; Cao, D. *Soft Matter* **2014**, *10* (35), 6844−6856.
(59) Tu, Y.; Lv, M.; Xiu, P.; Huynh, T.; Zhang, M.; Castelli, M.; Liu, Z.; Huang, Q.; Fan, C.; Fang, H.; Zhou, R. *Nat. Nanotechnol.* **2013**, *8* (8), 594−601.

DOI: 10.1021/acs.biomac.6b01674
Biomacromolecules 2017, 18, 797−807